Journal of Wind Engineering & Industrial Aerodynamics 190 (2019) 218–229

Contents lists available at ScienceDirect

Journal of Wind Engineering & Industrial Aerodynamics

journal homepage: www.elsevier.com/locate/jweia

An experimental study on the dynamic ice accretion processes on bridge cables with different surface modifications

Yang Liu [a], Wenli Chen [b], Yihua Peng [a,c], Hui Hu [a,*]

[a] Department of Aerospace Engineering, Iowa State University, Ames, IA, 50011-2271, USA
[b] School of Civil Engineering, Harbin Institute of Technology, Harbin, 150090, Heilongjiang, China
[c] School of Civil Engineering, Central South University, Changsha, 410100, Hunan, China

ARTICLE INFO

Keywords:
Cable-stayed bridge
Cable icing phenomena
Pattern-indented cable
Cable with helical fillets
Aerodynamic drag forces acting on cables

ABSTRACT

An experimental study was conducted to investigate the dynamic ice accretion processes on bridge cables with different surface modifications (i.e., 1. Standard plain, 2. Pattern-indented surface, and 3. Helical fillets). An Icing Research Tunnel available at Iowa State University (i.e., ISU-IRT) was used to generate two typical icing conditions (i.e., dry rime icing vs. wet glaze icing). During the experiments, while a high-speed imaging system was used to capture the transient behaviors of surface water transport and dynamic ice accretion processes over the surfaces of the cable models, a high-accuracy force measurement system was utilized to quantify the dynamic aerodynamic loadings acting on the cable models under different icing conditions. It was found that the addition of surface features (i.e., pattern-indented surface and helical fillets) could dramatically influence the dynamic ice accretion process and the final topology of the ice structures accreted on the cable surfaces. While the ice accretion on the standard plain cable and the cable with helical fillets was found to reduce the drag forces by about 25%, the ice accretion on the pattern-indented cable model would induce about 30% greater aerodynamic drag force acting on the cable model.

1. Introduction

Atmospheric icing has been widely recognized as a severe weather hazard to various engineering structures such as aircraft wings (Bragg et al., 2005), UAV propellers (Liu et al., 2019, 2018b), aero-engines (Dong et al., 2015; Li and Hu, 2017), wind turbines (Gao et al., 2019; Han et al., 2012), and power transmission lines (Ishihara and Oka, 2018; Liu et al., 2017). The ice accretion on these structures could essentially change the outer profiles of the original engineering designs, and degrade their aerodynamic performances. While the icing phenomena and the associated aerodynamic effects on aircraft and wind turbine applications have been extensively investigated (Gent et al., 2000; Parent and Ilinca, 2011), a relatively small volume of work is found in literature to address the icing problems related to civil engineering, especially the ice accretion on bridge cables, which is frequently observed on cable-stayed bridges located in cold regions (Demartino et al., 2015). Since most of the cable-stayed bridges are spanned over rivers or straits, where the air humidity is higher with periodical sprays, the stay cables for these bridges are more prone to encounter icing events when the ambient temperature is below zero. The ice accretion on bridge cables can be rime or glaze, depending on the weather conditions (Koss et al., 2012). Rime ice usually forms at the very cold temperatures when the impinged water droplets freeze immediately upon impacting on cable surfaces (Koss et al., 2012). Glaze ice usually forms at relatively warm conditions (i.e., temperatures just below zero), in which the impacted water mass would only freeze partially, while the remaining water coalesces into films/rivulets and runs back over the cable surfaces (Koss et al., 2012). As a result, the ice structures formed in glaze icing conditions are found to be very irregular and much more difficult to predict (Koss et al., 2012).

Ice accretion on bridge cables could cause undesirable large amplitude vibrations under wind action (Tan et al., 2016). As suggested by Koss and Lund (2013) and Koss et al. (2012), while different ice types were observed to form on the cable surfaces under different temperature conditions, the ice accretion could essentially influence the flow separation characteristics and hence the aerodynamic performance (i.e., the dynamic loading behaviors of the iced cable may only reflect a part of the clean dry cable behaviors). Further studies by Demartino et al. (2015) and Demartino and Ricciardelli (2015) revealed that the aerodynamic stability of bridge cables could be significantly affected by ice accretion. It was found that the diameter of cable cylinders could influence the ice accretion behavior and the corresponding aerodynamic forces

* Corresponding author.
E-mail address: huhui@iastate.edu (H. Hu).

https://doi.org/10.1016/j.jweia.2019.05.007
Received 21 March 2019; Received in revised form 26 April 2019; Accepted 13 May 2019

List of abbreviations and symbols

A_c	Ice accumulation parameter
C_D	Drag coefficient
D_1	Diameter of the standard plain cable model
D_2	Diameter of the cable model with pattern-indented surface
D_3	Diameter of the cable model with helical fillet
ε	The six standard deviations of the typical image noise
H^i_{ice}	Ice thickness accreted at the leading-edge of the cable models
I^0	Pixel intensity of the initial reference image of the cable models without water or ice
I^i	Pixel intensity of the acquired *i*th image as ice accreted over the cable surface
I^i_{diff}	The intensity difference maps for the images of the iced cable
ISU-IRT	Icing Research Tunnel of Iowa State University
K	The calibration constant in mm/pixel
LWC	Liquid Water Content
M1	Standard plain cable model
M2	Cable model with pattern-indented surface
M3	Cable model with helical fillet
Re	Reynolds Number
T_∞	Temperature of the incoming airflow
t_0	Time instant when the water spray is turned on
t	Time duration of the icing experiments
τ	The duration of the ice accretion process
V_∞	Incoming airflow velocity
x^i_0	Initial pixel locations of the leading-edge
x^i_{ice}	The advancing front of the ice layer accreted along the leading-edges of cable models
ρ_i	Ice density

(Demartino et al., 2015). Based on the quasi-steady approach, different models were developed to predict aerodynamic galloping stability of iced cables, which were systematically evaluated and compared in the work of Demartino and Ricciardelli (2015). Gjelstrup et al. (2012) also performed static and dynamic wind tunnel tests on a vertical cable cylinder with simulated thin ice accretion. The aerodynamic forces acting on the cylinder cable were obtained and the influence of surface roughness was examined (Gjelstrup et al., 2012). More recently, the wind-induced responses of inclined and yawed ice-accreted stay cable models were also revealed by Cao et al. (2018). It was found that the wind-induced response of the cable models could be enhanced along with the increase of ice thickness accreted on the cable surfaces (Cao et al., 2018). While the ice accumulation on the bridge cables could essentially change the outer profiles of the cables along with the dynamic surface water transport and ice accretion, the aeroelastic properties of the cables are suggested to be significantly affected, which may result in even more dangerous aeroelastic stability loss in comparison to those occurred in rain-wind conditions (Bosdogianni and Olivari, 1996; Hikami and Shiraishi, 1988; Li et al., 2010; Matsumoto et al., 1995, 1992).

It should be noted that before the icing-related large-amplitude-cable-vibration problem was raised with attention, many structural vibration damages have already been observed and studied in the cases of rain-wind induced vibrations (RWIVs) of bridge cables (Hikami and Shiraishi, 1988). In order to suppress the RWIVs, many surface modifications of the high-density poly ethylene (HDPE) sheathing have been introduced by bridge cable manufacturers, among which the HDPE tubing fitted with helical fillets and the HDPE tubing with pattern-indented surfaces are the two most prevailing approaches (Kleissl and Georgakis, 2012). Based on the previous researches on the RWIV mitigations by applying the different cable surface modifications (Gu and Du, 2005; Kleissl and Georgakis, 2012; Matsumoto et al., 1998), it was found that while the pattern-indented surfaces could effectively reduce the aerodynamic drag forces and promote the stabilization of the separated flows over the surface of the cable and to inhibit the formation of rivulets (Kleissl and Georgakis, 2012), the addition of helical fillets could drastically improve the aerodynamic properties and suppress the RWIVs of the tested cables (Christiansen et al., 2018; Gu and Du, 2005). Although the applications of pattern-indented surfaces and helical fillets have been demonstrated to be effective in improving the aerodynamic performance of bridge cables in the term of RWIV mitigation, the functionalities of these surface modification in icing conditions are not investigated until the recent work of Koss et al. (2013), in which the influence of icing on bridge cable aerodynamics was evaluated on three different full-scale samples of bridge cables with different cover tubes (i.e., standard plain, pattern-indented, and helical fillet). It was found that both the helical fillet and pattern-indented cables are less susceptible to the changes of cable surface morphology and ice accretion in comparison to the standard plain cable (Koss et al., 2013). However, these previous work only provided the icing images and the corresponding aerodynamic force data at the end-point of an icing process. There is no information available in literature to describe the transient behaviors of the surface water transport/ice accretion and the time-evolutions of aerodynamic forces acting on bridge cables during the dynamic ice accretion processes under different ambient temperature and liquid water content (LWC) conditions. In the present study, we aim to not only reveal the transient details of the surface water transport and ice accretion on the surfaces of bridge cable models under different icing conditions (i.e., rime *vs.* glaze), but also evaluate the effects of different surface modifications (i.e., standard plain, pattern-indented, and helical fillet) on the dynamic ice accretion processes and the corresponding aerodynamic responses of the bridge cable models.

The experimental study was performed in the unique Icing Research Tunnel of Iowa State University (ISU-IRT) with three full-scale samples of bridge cables (i.e., standard plain, pattern-indented, and helical fillet) being tested under two typical icing conditions (i.e., rime *vs.* glaze). In addition to achieving time-resolved measurements of the aerodynamic forces acting on the bridge cable models during the dynamic ice accretion processes, a high-speed imaging system was also used to capture the important ice accretion features and quantify the dynamic ice accretion rate over the surfaces of the different bridge cable models. The force measurements were correlated with the acquired ice accretion images to elucidate the underlying icing physics pertinent bridge cable icing phenomena.

2. Experimental setup and test models

2.1. ISU-Icing Research Tunnel (ISU-IRT)

In the present study, the icing experiments were carried out in the Icing Research Tunnel available at Aerospace Engineering Department of Iowa State University (i.e., ISU-IRT). As shown in Fig. 1, ISU-IRT has a test section of 2.0 m in length × 0.4 m in width × 0.4 m in height with four side walls being optically transparent. ISU-IRT has a capacity of generating a maximum wind speed of 60 m/s and airflow temperature of −25 °C. Based on the thermocouple measurements along and across the test section, it is found that the temperature distributions along and across the test section are quite uniform, with the maximum temperature difference being less than 1.0 °C. An array of 8 pneumatic atomizer/spray nozzles are installed at the entrance of the contraction section to inject micro-sized water droplets (10–100 μm in size) into the airflow. By

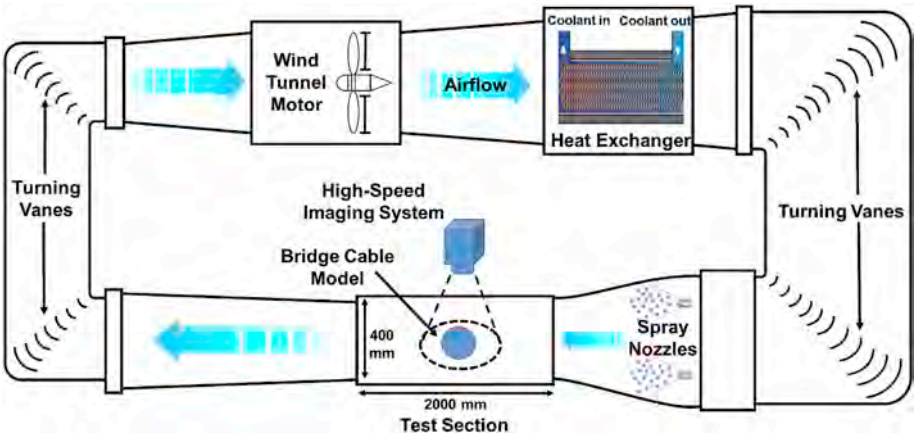

Fig. 1. A schematic of the Icing Research Tunnel available at Iowa State University (ISU-IRT).

manipulating the water flow rate through the spray nozzles, the liquid water content (*LWC*) in ISU-IRT could be adjusted (i.e., *LWC* ranging from 0.1 g/m^3 to 5.0 g/m^3). In summary, ISU-IRT can be used to simulate atmospheric icing phenomena over a range of icing conditions (i.e., from dry *rime* to extremely wet *glaze* ice conditions) (Liu et al., 2018a; Liu and Hu, 2018; Waldman and Hu, 2015).

2.2. Tested bridge cable models

Three sectional cable models were tested in the present study, which are: M1-standard plain cable model; M2-cable model with pattern-indented surface; and M3-cable model with helical fillet. All these test models are the original full-scale samples of real bridge cables supplied by bridge cable manufacturers. Fig. 2 shows the cable models and the corresponding application examples.

The cover tubes of the three cable models are all made of HDPE as those used in the previous studies (Kleissl and Georgakis, 2012; Koss et al., 2013). While M1 (i.e., the standard plain cable model) and M2 (i.e., the pattern-indented cable model) have the same outer diameter of 88 mm, M3 (i.e., the cable model with helical fillet) has a larger outer diameter of 105 mm. For the cable model with pattern-indented surface, the relative surface roughness is defined by the depth of the indentations, which was measured to be approximately 1% of the cable diameter. For the cable model with helical fillets, while the size of the fillets is the same with that in Kleissl and Georgakis (2012), which has a height of 3 mm and a width of 4 mm, the pitch length of fillets is about $16D_3$ (i.e., 1680 mm with an angle of 11.1°). It should be noted that, the diameter of the test models is the base diameter, i.e., the diameter of the pattern-indented cable model does not consider the depth of the indentations; the diameter of the cable model with helical fillet does not consider the thickness of the helical fillet.

2.3. Experimental setup

Fig. 3 shows the schematic of the experimental setup used in the present study to quantify the dynamic ice accretion processes on the cable models. As shown schematically in Fig. 3, the test cable model was mounted horizontally in the middle of ISU-IRT test section, supported by a stainless-steel rod. It should be noted that, while the cable model spans over the entire width of the test section, no end plate was used during the icing experiments. The angle of attack (AoA) of the test model was adjustable by pivoting the test model about the supporting rod and fixing it at the desired angles as measured with a digital inclinometer. Following a careful calibration procedure of the ISU-IRT, the wind speed

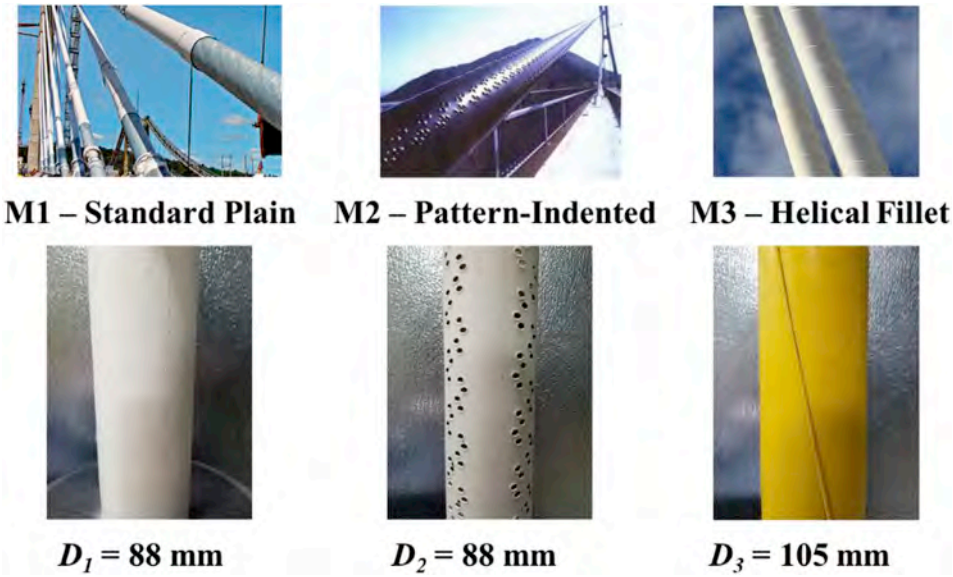

Fig. 2. Tested bridge cable models used in the present study (M1: standard plain cable model; M2: cable model with pattern-indented surface; and M3: cable model with helical fillet).

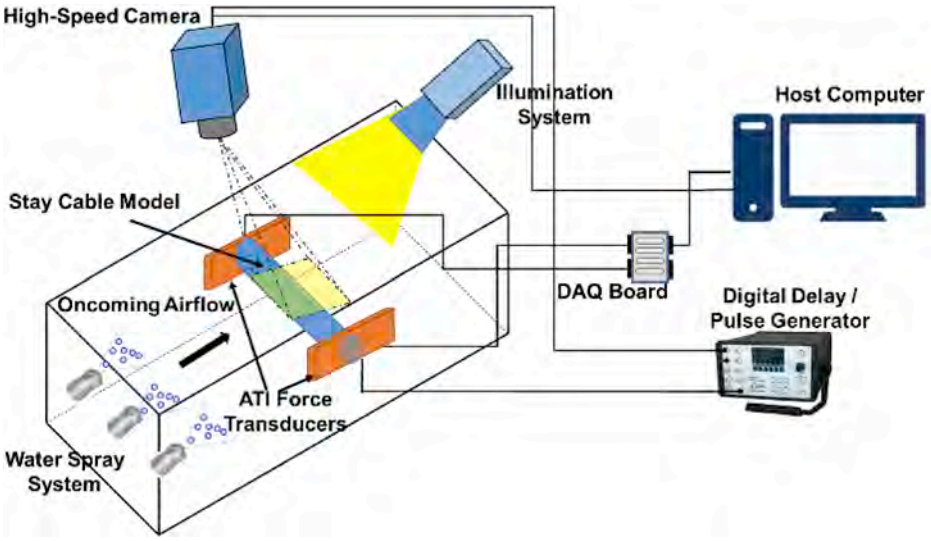

Fig. 3. A schematic of the experimental setup used to quantify the dynamic ice accretion processes and the corresponding aerodynamic forces acting on the different bridge cable models.

and loading condition in the test section are confirmed to be very uniform. By adjusting the spray nozzle parameters (i.e., input air pressure and water pressure), the uniformity of the ice accretion across the test section is checked before each icing experiment (i.e., the spray system would be adjusted to make sure a uniform ice distribution across the entire test section) as also reported in our previous icing experiments (Gao et al., 2019; Li et al., 2019; Liu et al., 2019). A high-resolution high-speed imaging system (i.e., PCO Tech, PCO-Dimax S4, up to 1279 frames per second @ 2016 pixels by 2016 pixels) along with a 60 mm Macro-lens (Nikon, 60 mm Nikkor2.8D) was used in the present study to record the dynamic ice accretion process over the surfaces of the test models. The spatial resolution of the high-speed imaging results is 0.088 mm/pixel for the present study. The camera was positioned normal to the test model. Low-flicker illumination was provided by a pair of 100 W Studio-LED light Units (RPS Studio Light, Model RS-5610 and RS-5620).

In addition to acquiring the ice accretion images, a high-accuracy dual-transducer force measurement system (i.e., consists of two sets of high-sensitive, multi-axis force-moment transducers, i.e., ATI-IA Mini 45, mounted at the two ends of the test model) was also used to measure the aerodynamic drag forces acting on the test models during the dynamic ice accreting processes. The force/moment transducers are composed of foil strain gage bridges, which can measure the forces on three orthogonal axes, and the moment (torque) about each axis. The precision of the force-moment transducers for force measurements is ±0.04% of the full range (290 N). During the experiments, the force/torque transducers were synchronized via a 16-bit data acquisition system (NIUSB-6218) for the data acquisition up to 5000 Hz. The measurement results of the force/moment transducers were used to determine the aerodynamic performance of the bridge cable models in the term of drag coefficients (i.e., C_D), which is defined as $C_D = F_D/\left(\frac{1}{2}\rho_a V_\infty^2 S\right)$, where F_D is the drag force acting on the test model, ρ_a is the density of air, V_∞ is the velocity of the incoming airflow, and S is the relevant surface area of the test model (i.e., $S = D{\cdot}L$ with D being the diameter and L being the spanwise length of the test model), respectively. Since the test model was mounted horizontally (i.e., perpendicular to the direction of the incoming airflow) in the ISU-IRT during the ice accretion experiments, the drag force, F_D, can be measured directly by adding the measured values of the horizontal components of the aerodynamic forces acting on the test model. The gaps between the ends of the test model and the adjacent walls of wind tunnel were carefully controlled to be less than 0.10% of the span-length of the test model, as suggested by Nilanjan (1999). The measurement uncertainty caused by the gaps between the model ends and the walls of the wind tunnel is therefore controlled to be less than 2% (Nilanjan, 1999). The effects of the model blockage, the wind tunnel walls and wake interferences on the measurement results were also calibrated by using the methods described in Barlow et al. (1999). Under each icing condition, the experiments were repeated multiple times (3–5 times), and the measured drag coefficients under the same icing condition were compared quantitatively. It was found that, the variation of the measured drag coefficients was less than ~8% in each icing condition.

2.4. Test cases

In the present study, both rime and glaze ice accretion conditions were generated in the ISU-IRT. While the incoming airflow velocity was kept constant at $V_\infty = 18$ m/s, referenced based on the field measurements of Fukusako et al. (1989), different ambient air temperatures (i.e., −5 °C and −15 °C) and LWC levels (i.e., 1.0 g/m^3 and 3.0 g/m^3) were achieved for the case design as shown in Table 1.

It should be noted that, while the velocity of the oncoming airflow was set to be 18 m/s to represent the typical wind condition in real situations, the corresponding Reynolds number in the present study is 1.25×10^5 for M1 and M2, and 1.50×10^5 for M3. Since the cable-stayed bridges are usually located at low altitude, they are more prone to encounter high-water-content conditions (e.g., freezing drizzle/rain and ocean spray). The LWC level for bridge cable icing is suggested to be much higher than that of aircraft in-flight icing conditions (<1.0 g/m^3) (Battisti, 2015). In the present study, the LWC was adjusted from 1.0 g/m^3 to 3.0 g/m^3 to simulate different icing conditions as suggested in Appendix C (Anon, 2013).

Table 1
Test cases in the present study.

Case No.	Cable Model	V_∞ (m/s)	T_∞ (°C)	LWC (g/m^3)
1	M1	18	−5	3.0
2	M1	18	−15	1.0
3	M2	18	−5	3.1
4	M2	18	−15	1.0
5	M3	18	−5	3.0
6	M3	18	−15	1.0

3. Measurement results and discussion

3.1. Aerodynamic force measurements of the "clean" bridge cable models

Before conducting the icing experiments, the reference aerodynamic drag forces of the "clean" bridge cable models (i.e., without any ice accretion over the surfaces of the test models) were first measured by using the dual-transducer force measurement system. The measured drag coefficient data is used as the baseline to evaluate the effects of ice accretion on the aerodynamic loadings acting on the cable models.

Fig. 4 shows the measurement results of the drag coefficients of the different bridge cables without any ice accretion. The previous experimental data (curves) of drag coefficients as a function of Reynolds number for the cable models with the same surface modifications (Kleissl and Georgakis, 2012) are also plotted in Fig. 4 for quantitative comparisons. It can be seen clearly that, at the airflow velocity of $V_\infty = 18$ m/s (i.e., $\mathrm{Re} = 1.25 \times 10^5$ for M1 and M2, and $\mathrm{Re} = 1.50 \times 10^5$ for M3), the measured drag coefficient data (i.e., indicated by the circle marker for M1, the rectangular marker for M2, and the triangle marker for M3) in the present study agrees very well with that given in Kleissl and Georgakis (2012). Based on the quantitative comparison given in Fig. 4, it is validated that while the dual-transducer force measurement system is very accurate in measuring the aerodynamic forces acting on the bridge cable models, the flow conditions in the ISU-IRT is consistent with those in the previous studies (Kleissl and Georgakis, 2012; Koss et al., 2013).

3.2. High-speed imaging of the dynamic ice accretion processes over the different bridge cable models

After measuring the aerodynamic forces of the "clean" cable models, the refrigeration system of the ISU-IRT was switched on to produce the different ice accretion conditions to examine the dynamic icing processes on the different bridge cable models and the corresponding aerodynamic forces acting on the cable models induced by the ice accretion. To perform the ice accretion experiment, the ISU-IRT was operated at prescribed frozen-cold temperature levels (e.g., $T_\infty = -15\,^\circ$C for the rime icing case and $T_\infty = -5\,^\circ$C for the glaze icing case) for at least 30 min without turning on the water spray system to ensure that the ISU-IRT reached a thermal steady state before the icing experiments. After switching on the water spray system, the supper-cooled water droplets carried by the frozen-cold airflow would impinge onto the surface of the test model to start the dynamic ice accreting process.

Fig. 5 shows the typical snapshots of the dynamic ice accretion processes over the different bridge cable models under the test condition of

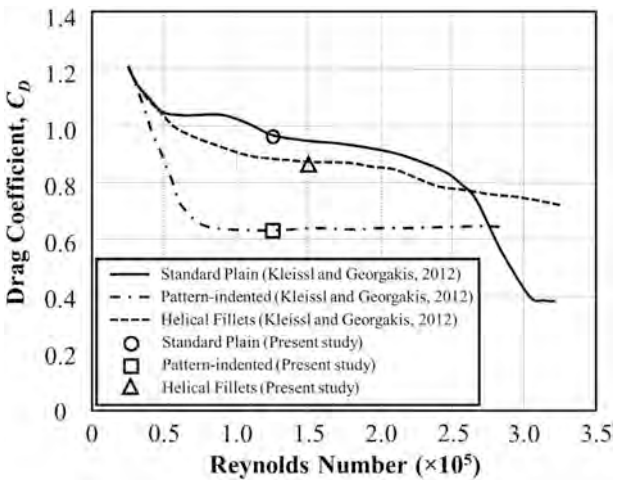

Fig. 4. The measured aerodynamic drag coefficients of the "clean" bridge cable models and comparison with the drag coefficient data as a function of Reynolds number given in Kleissl and Georgakis (2012).

freestream airflow velocity $V_\infty = 18$ m/s, $LWC = 1.0$ g/m^3, and the ambient temperature $T_\infty = -15\,^\circ$C. As the super-cooled water droplets impacted on the cable surfaces under such a cold condition, the heat transfer process would be sufficiently fast to dissipate all the latent heat of fusion released during the phase changing (i.e., solidification) process of the impinged super-cooled water droplets. The ice accretion over the surfaces of the cable models was found to exhibit typical *rime* characteristics (i.e., with milk-white and opaque appearances), similar as those described in the previous study of Hansman and Kirby (1987).

As shown clearly in Fig. 5(a), when the super-cooled water droplets impinged onto the cable model with standard plain surface (i.e., M1), due to the uniform surface finish over the cable model, the impinged water droplets would just freeze instantly with an ice layer formed along the stagnation region, i.e., the ice thickness distribution is dependent on the water collection efficiency around a cylinder (Papadakis et al., 1989). It is found that, while the ice accreting surface becomes relatively rough due to the small air bubbles being trapped between the frozen ice grains, the accreted ice layer conforms well to the cylinder profile of the cable model. As the time goes by, with more and more super-cooled water droplets impinged and froze on the bridge surface, the ice layer accreted along the leading-edge of the cylinder cable was found to become thicker and thicker, as shown clearly in Fig. 5(a). It should be noted that, along with the thickening of the leading-edge ice thickness, some noticeable ice "feathers" were also found to be generated at the edge of the icing region. Due to the immediate freezing of the water droplets upon impingement, no water mass would run back. Therefore, no ice was found to accrete beyond the direct impact zone of the super-cooled water droplets.

For the ice accretion process over the cable model with pattern-indented surfaces (i.e., M2) under the same rime icing condition, similar ice features are observed as shown in Fig. 5(b). It should be noted that, although the surface of M2 is textured with the indented patterns, the distribution of ice accretion on the cable surface is very similar to that on M1. The impinged super-cooled water droplets were found to freeze immediately upon impact, regardless of the surface textures. Due to the relatively small ratio between the indentation depth and the cable diameter (i.e., approximately 1%), the ice thickness distribution was also principally determined by the water collection efficiency. However, different from the ice accretion over the standard plain surface, the ice accretion over the pattern-indented surface was found to have larger and more evident ice roughness features due to the existence of the indentations. While the super-cooled water droplets impinged onto the cable surface, some of them were found to freeze instantly in the indentations. As the time goes by, the ice accreting cable surface was found to become smoother, especially the stagnation region where the indented-pattern located before the ice accretion, as shown in Fig. 5(b). It is also found that, though the indented patterns have a great impact on the boundary layer flow and the local convective heat transfer (Hansman et al., 1991), the ice accretion process seems almost the same with that over the standard plain surface due to the immediate freezing mechanism.

When the super-cooled water droplets impinged on the cable model with helical fillet (i.e., M3), the ice mass distribution over the cable surface is found to be changed greatly as clearly shown in Fig. 5(c). Due to the rapid heat transfer under this test condition, the impinged water droplets would freeze immediately upon impacting on the cable surface. Since the height of the helical fillet is much larger (i.e., 3 mm) than the airflow boundary layer thickness around the leading-edge area of the cable model, the water droplets carried by the incoming airflow can be easily caught by the helical fillet and frozen along the fillet as shown in Fig. 5(c). While the impinged water droplets were blocked by the helical fillet with more ice accreting along the front surface of the fillet, almost no water mass was found to reach to the regions behind the fillet. Thus, as more and more water impinged and froze on the cable surface, a fillet-guided ice accretion was formed as shown in Fig. 5(c). It is also found that, due to the helical distribution of the fillet, the amount of ice accretion along the fillet front would vary along the span, i.e., more ice

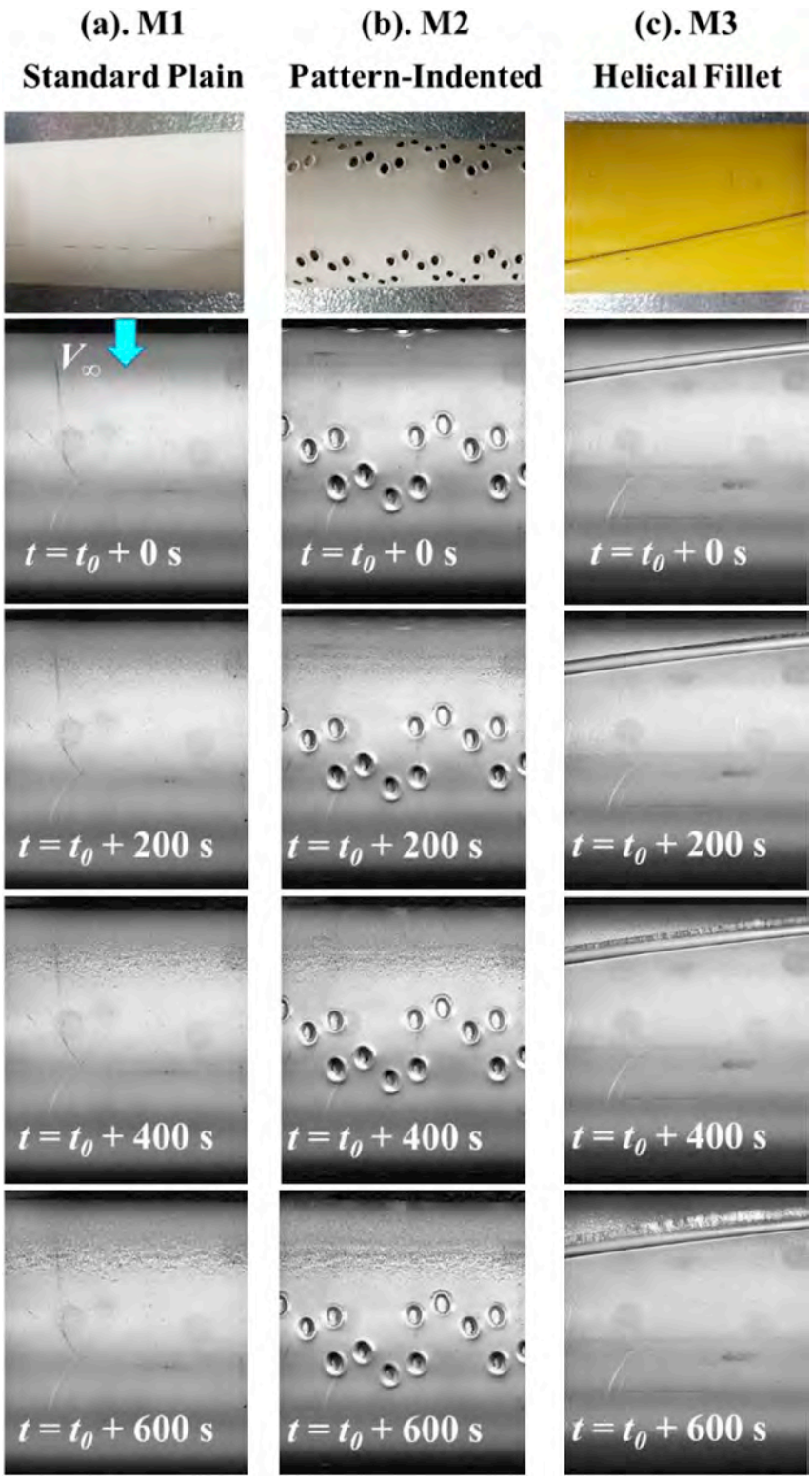

Fig. 5. Acquired snapshots to reveal the dynamic ice accretion processes on the different bridge cable models under the rime icing condition.

would be formed on the fillet front when the fillet is closer to the leading-edge due to the larger water collection efficiency. However, it should be noted that the blockage effect (i.e., capability of catching the water droplets) of the fillet would be reduced when the fillet approaches very close to the leading-edge (i.e., as the projected area of the fillet is overlaid by the projected area of the direct water impingement region perpendicular to the incoming airflow). Since the ice accretion over the cable surface is redistributed, with a substantial amount of ice accreted along the helical fillet, the boundary layer airflow and the aerodynamic forces acting on the cable model are suggested to be altered significantly in comparison to those in the cases of the standard plain cable and the pattern-indented cable.

Fig. 6 shows the typical snapshots of the dynamic ice accretion processes over the different bridge cable models under the test condition of

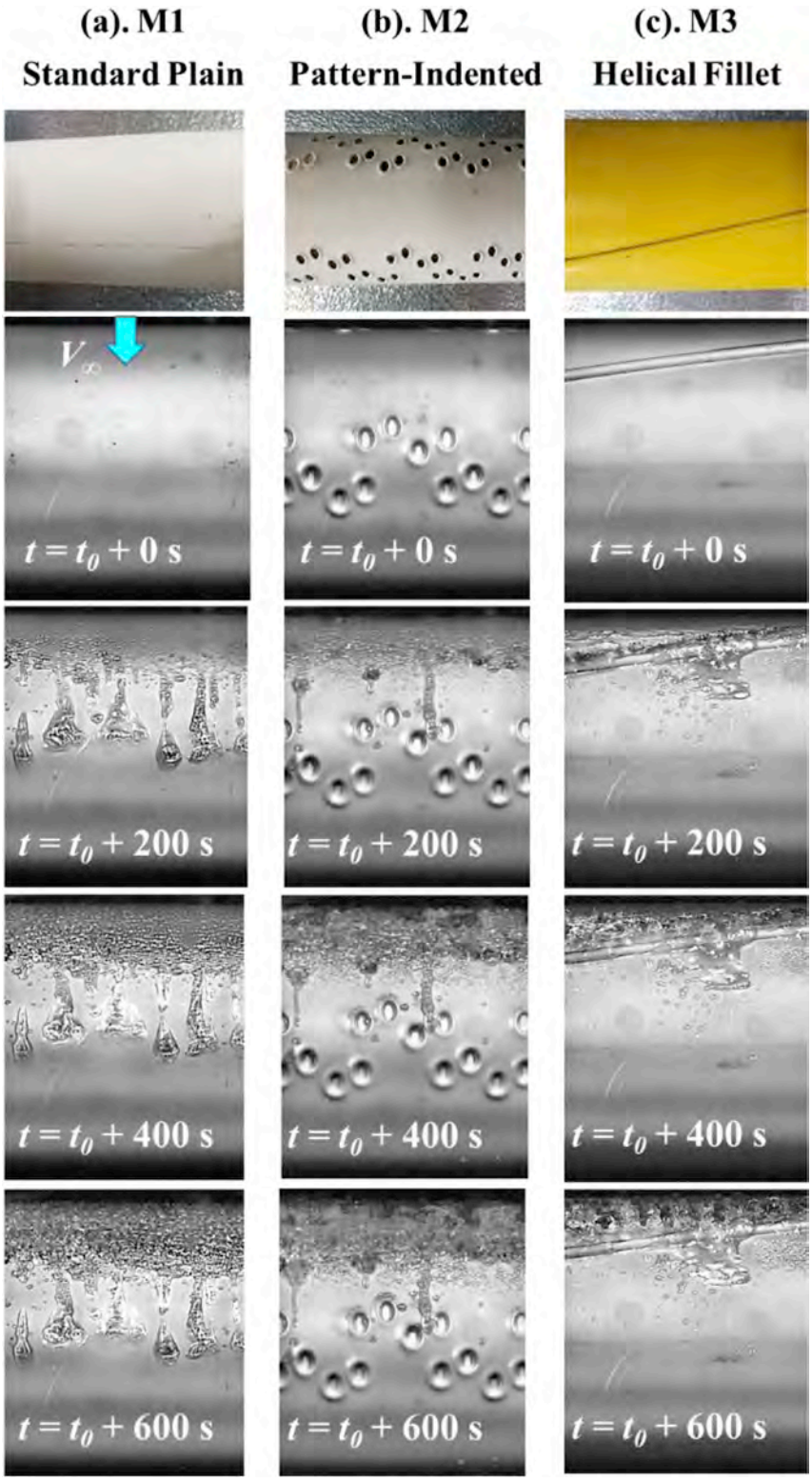

Fig. 6. Acquired snapshots to reveal the dynamic ice accretion processes on the different bridge cable models under the glaze icing condition.

freestream airflow velocity $V_\infty = 18$ m/s, $LWC = 3.0$ g/m^3, and the ambient temperature $T_\infty = -5$ °C. In comparison to the rime icing cases in Fig. 5, much more supercooled water droplets would impinge onto the cables within the same duration of the ice accretion experiment. Due to the much warmer temperature for this test case, the heat transfer process would not be fast enough to remove all the released latent heat of fusion during the solidification process of the impinged super-cooled water droplets. As a result, only a portion of the supercooled water droplets would be frozen and solidified upon impact, while a large portion of the impinged water mass would still be in liquid state and flow freely over the cable surfaces. Thus, the ice accretion over the cable surfaces under this test condition was found to be a typical glaze ice accretion process (Hansman and Kirby, 1987).

As shown clearly in Fig. 6(a), when the super-cooled water droplets

impinged onto the cable model with standard plain surface (i.e., M1), a water film was found to form rapidly over the ice-accreting cable surface. Due to the aerodynamic shear force exerted by the boundary-layer airflow, the impinged water mass was found to be transported away quickly from the direct impingement zone of the supercooled water droplet (i.e., the region near the leading edge of the cylinder cable). As driven by the boundary-layer airflow, the unfrozen surface water was found to run back over the cable surface and form into the rivulets, as also reported in Waldman and Hu (2015). These runback rivulets were eventually frozen at further downstream beyond the direct impingement zone of the supercooled water droplets. As a result, the ice accretion over the cable surface under this test condition was found to extend much further downstream over the cable surface.

Fig. 6(b) shows the ice accretion process over the cable model with pattern-indented surfaces (i.e., M2) under the same glaze icing condition. It can be seen clearly that, while similar ice features were generated on the surface of M2, the appearance of the accreted ice layer was very different from that over the standard plain surface, i.e., M1. Since the ice accretion process under this test condition was essentially determined by the heat transfer properties over the cable surface, the existence of the indented patterns was suggested to significantly enhance the convective heat transfer (Hansman et al., 1991), thereby affect the icing mechanism and final ice structures. It is found that while the ice formation on M1 appears to be very transparent and clear, the ice structures formed on M2 seems to be more opaque with larger roughness.

Fig. 6(c) shows the ice accretion process over the cable model with helical fillet (i.e., M3). It is clearly seen that as the large amount of water impinged onto the cable surface, the water transport behavior was significantly altered by the helical fillet. While partial of the impinged super-cooled water droplets was frozen along the fillet, the remaining water mass was found to be transported along the helical fillet, generating a surface water flow not only in the streamwise direction, but also in the spanwise. Thus, the ice accretion on this type of cable would become much more complicated, involving a three-dimensional motion of the surface water/ice that is closely coupled with the dynamically evolving boundary layer airflow and convective heat transfer. As a result, very irregular ice structures were formed along the helical fillet. It should be noted that, when the thickness of the surface water goes beyond the height of the fillet as more and more water droplets are collected on the cable surface, "breaking of dike" would occur with a portion of the surface water being transported over the helical fillet, driven by the strong shear stress exerted by the airflow.

3.3. Further analysis about the ice accretion process on the different bridge cable models

In the present study, further efforts were made to quantify the thickness of ice layers accreted along the leading-edge of the different bridge cable models as a function of time. The acquired ice accretion images are actually the maps of light intensity scattered or reflected from the surfaces of cable models, impinged water mass, and accreted ice. By deriving the changes of the intensity maps in time sequences, Waldman and Hu (2015) developed an image processing algorithm to extract the leading-edge ice thickness variation during the dynamic ice accretion process. In the present study, we applied a modified image processing algorithm (Liu et al., 2018c) to extract the time-histories of the leading-edge ice thickness variations on the different cable models during the dynamic ice accretion processes.

As described in Waldman and Hu (2015) and Liu et al. (2018c), the initial reference image of the cable models without water or ice was defined as I^0, and the acquired ith image as ice accreted over the cable surface was defined as I^i. The intensity difference maps for the images of the iced cable, thus, can be derived as:

$$I^i_{diff} = I^i - I^0 \tag{1}$$

By conducting such an image processing procedure, the pixel counts in the intensity difference maps would contain the information about the image changes from the initial state (i.e., cable surface without water or ice) to the presence of water or ice accretion. Therefore, the advancing front of the ice layer accreted along the leading-edges of cable models can be identified at every spanwise position y,

$$x^i_{ice} = \text{first}\left(I^i_{diff}(x)^2 > \varepsilon\right) \tag{2}$$

where ε was chosen as the six standard deviations of the typical image noise for the present study. The image noise was characterized by calculating the root-mean-square (rms) values of the pixel fluctuations in the blank areas of the images (i.e., areas excluded cable, ice, or water) before ice accretion.

Knowing the initial pixel locations of the leading-edge, i.e., x^i_0, the ice thickness accreted at the leading-edge of the cable models can be calculated:

$$H^i_{ice} = K\left(x^i_{ice} - x^i_0\right) \tag{3}$$

where K is the calibration constant in mm/pixel.

By applying the image processing method described above, the actual ice thickness accumulated along the leading edge of the cable models

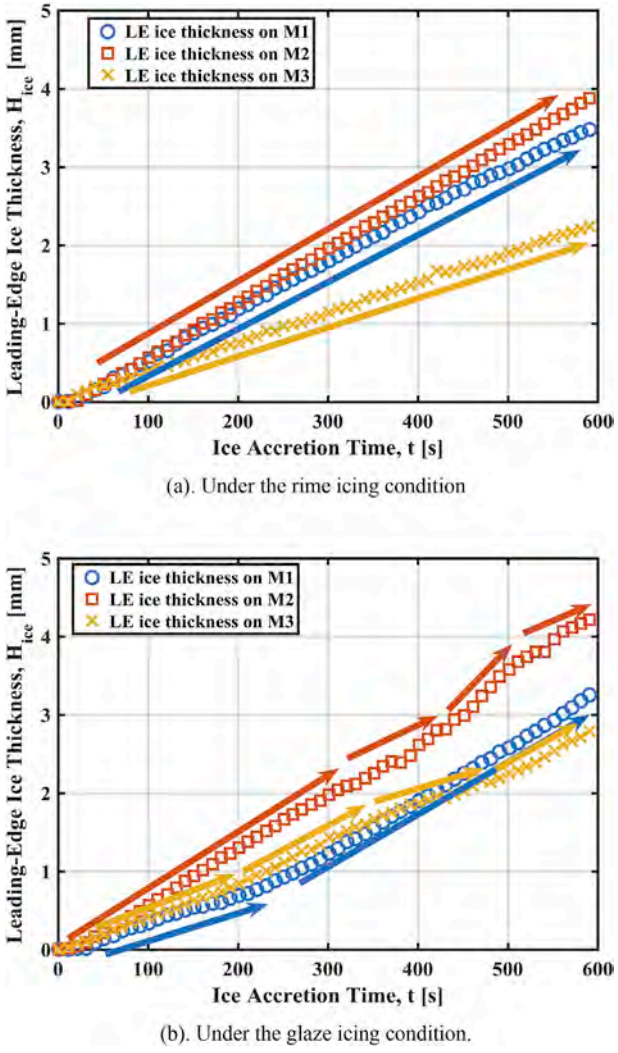

(a). Under the rime icing condition

(b). Under the glaze icing condition.

Fig. 7. Time histories of the leading-edge ice thickness accreting on the different bridge cable models under (a) the rime icing condition and (b) the glaze icing condition.

were quantitatively extracted. Fig. 7 shows the time histories of the measured ice thickness accreted along the leading-edge of the different bridge cables. As can be seen clearly in Fig. 7(a), under the rime icing condition, while the thickness data of the ice layers accreted on the cable models shows a linear increase during the icing processes, there is a discrepancy of the ice growth rate on the different cable models. As suggested by Anderson (2001), the ice accumulation parameter, A_c, is defined as:

$$A_c = \frac{\mathrm{LWC} \cdot V_\infty \cdot \tau}{D \cdot \rho_i} \tag{4}$$

where τ is the duration of the ice accretion process, D is the diameter of the cylinder cable model, and ρ_i is the ice density. Thus, the time derivative of the ice accumulation parameter can be calculated to estimate the growth rate of the ice layers accreted on the cable models, that is:

$$\frac{dA_c}{dt} = \frac{\mathrm{LWC} \cdot V_\infty}{D \cdot \rho_i} \tag{5}$$

It is obvious that, while the environmental conditions, i.e., the incoming airflow velocity, V_∞, and LWC, are kept constant, the ice growth rate would be inversely related to the diameter of the cable model, which is confirmed by the measured ice thickness data given in Fig. 7(a), i.e., the leading-edge ice growth rates on the standard plain cable (M1 with diameter of 88 mm) and the pattern-indented cable (M2 with diameter of 88 mm) are found to be much faster than that on the cable model with helical fillet (M3 with diameter of 105 mm). It should be noted that, while M1 and M2 have the same diameter and are exposed in the same icing condition, the leading-edge ice growth rate on M2 is found to be slightly faster than that on M1, i.e., 0.0067 mm/s for M2 *vs.* 0.0058 mm/s for M1. It is suggested that the discrepancy of the ice growth rate is essentially due to the surface modification, i.e., pattern-indented textures along the leading-edge, which changes the distribution of water collection efficiency (Shin, 1996) with more water droplets being caught and frozen in the indentations. For the ice accretion on M3, however, though the cable surface is featured by the helical fillet that can redistribute the water collection and ice accretion along the fillet, the leading-edge ice accretion is almost not affected. The slower leading-edge ice growth rate on M3 is principally due to the larger diameter of the cable model.

Fig. 7(b) shows the time histories of the leading-edge ice thickness variations on the different cable models under the glaze icing condition. It is clearly seen that, although much more water mass would impinge onto the cable surfaces within the same duration of ice accretion under this condition, the leading-edge ice thickness is found to only change slightly in comparison to those obtained in the rime icing cases. Due to the relatively warm airflow temperature, and large amount of the water impingement, the heat transfer is not sufficient to remove all of the latent heat of fusion in the impinged water mass. Only partial of the impinged water mass would be frozen upon impacting on the cable surfaces, with the remaining being transported and frozen downstream. Due to the very complex surface water transport and ice accretion processes on the different models, the time variations of the leading-edge ice thickness are found to be very different from those derived in the rime icing condition. While the leading-edge ice thickness increases monotonously during the ice accretion processes, there are evident non-linear features being observed in the ice growth curves as shown in Fig. 7(b). For the standard plain cable, M1, it is found that the leading-edge ice thickness would increase linearly in the beginning stage, i.e., $t < 200$ s, with a growth rate of 0.0035 mm/s. However, this ice growth rate is much slower than that in the rime condition (i.e., 0.0058 mm/s), which is suggested to be caused by the significant surface water runback. As the time goes by, along with the formation of ice roughness around the stagnation region, the impinged water droplets are more likely to be caught and frozen locally, as indicated by the increased leading-edge ice growth rate, i.e., 0.0066 mm/s. For the pattern-indented cable, M2, although its diameter is the same with M1, the thickness of the ice layer accreted along the leading-edge is found to be obviously larger in comparison to that on M1. It is suggested that the thicker ice layer formed along the pattern-indented lead-edge is essentially due to the enhanced the convective heat transfer, which is caused by the rough/indented surface textures (Hansman and Turnock, 1989). The fluctuation of the ice growth rate is suggested to be caused by the changing ice roughness features accreted along the cable leading-edge during the dynamic ice accretion process. For the cable model with helical fillet, M3, though its diameter is larger than M1, the ice thickness accreted along the leading-edge is found to be almost the same with that on M1 in the first 400 s of ice accretion, which is suggested to attribute to the slower surface water runback as trapped by the helical fillet as shown in Fig. 6(c). As more and more water mass is collected on the cable surface, the runback surface water would go beyond the helical fillet, with less water mass being trapped and frozen locally along the leading-edge region, resulting in a slower ice growth rate along the leading edge as indicated clearly in Fig. 7(b).

3.4. Time-evolutions of the aerodynamic drag coefficients of the ice accreting bridge cable models

In the present study, the aerodynamic forces were acquired continuously for more than 600 s with the water spray system being switched on to enable ice accreting dynamically over the different bridge cable models under both the rime and glaze conditions. Fig. 8 shows the measured drag coefficient data, C_D, of the different cable models under the rime icing condition. The Gaussian-filtered mean values and the ± 1.5 standard deviation (STD) bounds of the instantaneous measurement results were also given in the plot for comparison.

As can be seen clearly in Fig. 8(a), at the beginning of the ice accretion process, the mean drag coefficient of the standard plain cable is about $C_D = 0.98$, which is consistent with that measured in the previous study (Kleissl and Georgakis, 2012). During the first 100 s of ice accretion, the mean drag coefficient of the cable model was found to be almost not changed, which indicates that the slight increase of the leading edge ice layer at the beginning stage has little effect on the aerodynamic drag of the cable model. As the time goes by, the mean drag coefficient of the cable model was found to decrease to $C_D = 0.75$ after $t = 200$s. Though the thickness of ice layer is continuously increasing from $t = 200$s to $t = 600$s, the mean drag coefficient is found to be kept the same during this period. It is suggested that the decrease of the drag coefficient of M1 during the ice accretion process is due to the change of the leading edge profile from the original circle radius to the streamlined ice layer. Meanwhile, the formation of the ice roughness would also contribute to the drag reduction due to the transition of the boundary layer airflow. It should also be noted that, along with the reduction of the mean drag coefficient, the fluctuation amplitude of the drag coefficient is found to be significantly reduced, which is suggested to be caused by the smaller separation region in the wake as the profile of the ice accreting cable model becomes more streamlined.

For the pattern-indented cable model, M2, however, the mean drag coefficient is found to increase as the time goes by as clearly shown in Fig. 8(b). As mentioned above, the original indented textures are actually roughness elements that can trigger an earlier transition of the boundary layer airflow. As the ice accretes over the indented patterns, the original roughness patterns would be covered by the ice layer, thereby postpone the boundary layer transition. As a result, the drag coefficient of M2 is found to increase during the ice accretion process. The time evolution of the drag coefficient of M3 is very similar to that of M1 as shown in Fig. 8(c). It is suggested that the ice layer accreted along the helical fillet has a very small effect on the aerodynamic drag force. The growing ice along the fillet would only extend the width of the fillet, but contribute little to the aerodynamic drag. The formation of the leading edge ice layer, however, would dramatically change the outer profile of the cable, resulting in the decrease of the mean drag coefficient. Similar to that in the case of M1, the fluctuation amplitude of the drag coefficient of M3 is

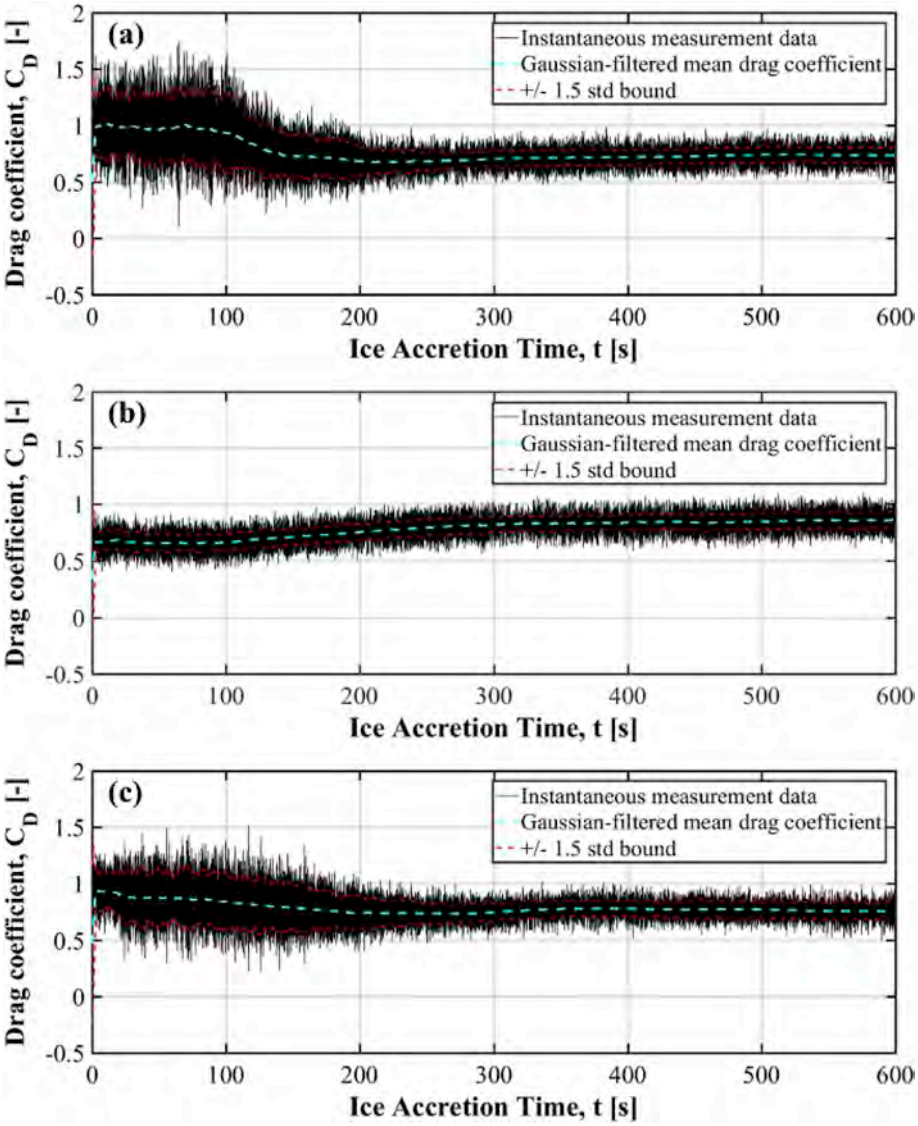

Fig. 8. Time-evolutions of the aerodynamic drag coefficients of the ice accreting bridge cable models under the rime icing condition (a) M1, standard plain; (b) M2, pattern-indented; (c) M3, helical fillet.

also found to be significantly reduced during the icing process, due to the formation of the more streamlined leading edge as ice accretes. It should be noted that, in addition to the changes of the drag coefficient caused by the ice accretion on the cable surfaces, the aeroelastic properties of the cables would also be significantly affected due to the elongation of the outer profiles of the ice accreting cable models, which may result in further amplified galloping and potential collapse.

Fig. 9 shows the time evolutions of the aerodynamic drag coefficients of the different cable models during the dynamic ice accretion processes under the glaze icing condition. As described above, the ice accretion process would be very complicated under this condition, with evident surface water transport and irregular ice structure formation over the cable surfaces. As a result, the drag force generated by the ice accretion is found to be very different from that in the rime condition. As clearly shown in Fig. 9(a), when ice builds on the standard plain cable, M1, the drag force is found to decrease quickly within the first 30 s of ice accretion. It is suggested that this rapid decrease of the drag force at the early icing stage is essentially caused by the change of the boundary layer airflow as the impinged water mass transported over the cable surface. As the time goes by, the ice structures formed on the cable surface are found to become larger and larger, which can dramatically disturb the airflow and increase the aerodynamic drag. It is found that after 600 s of ice accretion, the drag force of M1 is almost the same with that of the "clean" cable model. Fig. 9(b) shows the time history of the drag coefficient of M2 during the dynamic ice accretion process. Similar to that in the rime icing condition, the drag coefficient of the cable model is also found to increase gradually as the ice accretes. However, it should be noted that at the beginning stage of ice accretion process, there is also a slight decrease of the drag coefficient that is due to the change of boundary layer airflow as the surface water appears. Similar phenomenon is also observed in the case of M3. However, different from the other two cable models, the fluctuating amplitude of the drag force is also found to increase greatly along with the increase of the mean drag force, as shown in Fig. 9(c). It is suggested that, the amplifying drag fluctuation is essentially caused by the rapid growth of the irregular ice structures along the helical fillet.

4. Conclusions

An experimental study was conducted to investigate the dynamic ice accretion processes on the surfaces of bridge cables with different surface modifications (i.e., 1. Standard plain, 2. Pattern-indented surface, and 3. with helical fillets). The icing experiments were performed in the unique

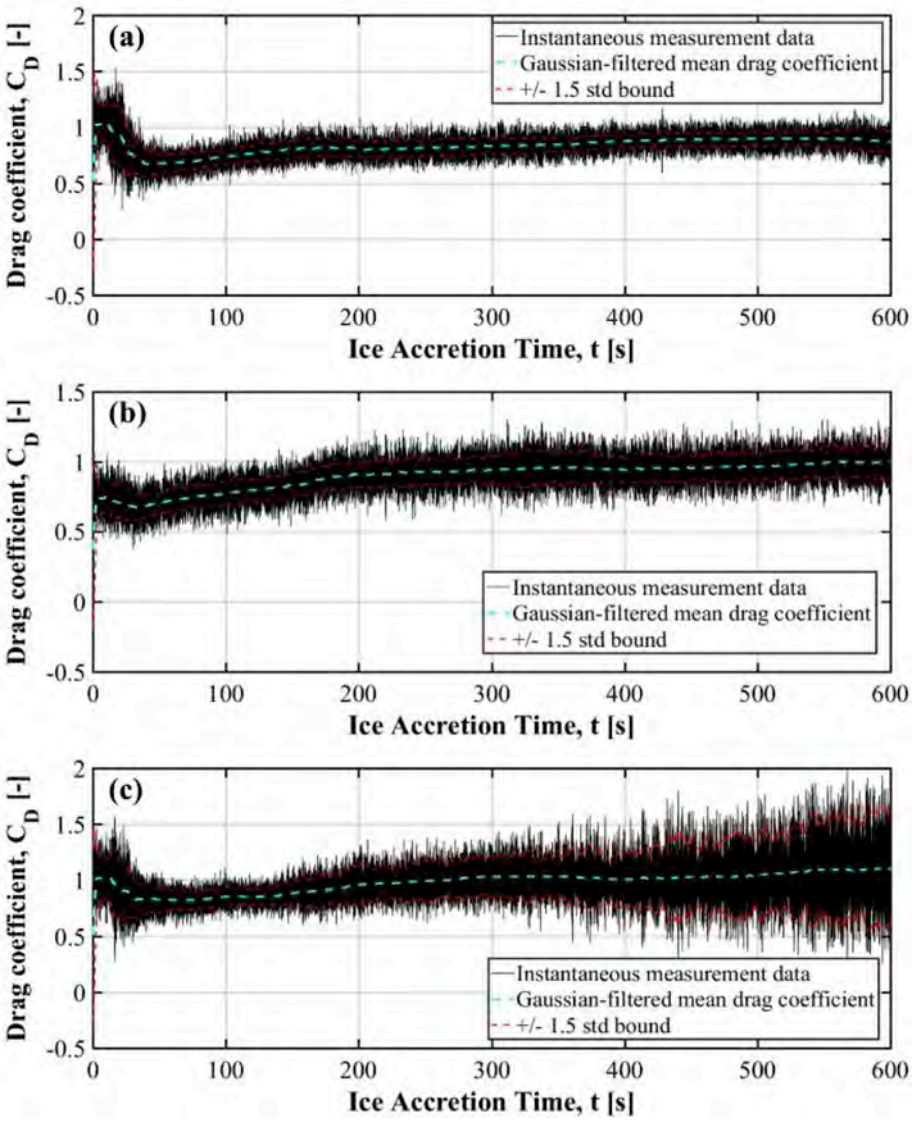

Fig. 9. Time-evolutions of the aerodynamic drag coefficients of the ice accreting bridge cable models under the glaze icing condition (a) M1, standard plain; (b) M2, pattern-indented; (c) M3, helical fillet.

Icing Research Tunnel available at Iowa State University (i.e., ISU-IRT). In addition to revealing the transient details of the dynamic ice accretion processes by using a high-speed imaging system under the different icing conditions (i.e., rime *vs.* glaze), the time-evolutions of the aerodynamic drag forces acting on the cable models with different surface features were also characterized by using a high-accuracy force measurement system.

It was found that, while the dynamic ice accretion process would be greatly affected by the surface modifications (Pattern-indented surface *vs.* helical fillets), the resultant aerodynamic drag forces were also found to be influenced substantially by the different surface features. Under the typical rime icing condition, while the pattern-indented surface was found to have little effects on the overall ice accretion distribution, the helical fillets were found to greatly redistribute the ice mass, with substantial ice structures accreted along the helical fillet. Under the wet glaze icing condition, the surface modifications, either the pattern-indented surface or the helical fillet, were found not only to redistribute the water collection and ice accretion, but also to affect the boundary layer airflow and heat transfer, thereby, further influence the morphology of the ice structures accreted over the cable surfaces. By extracting the time-histories of the thickness variations of the ice layers accreted at cable leading-edges under different icing conditions, it was found that, while the accreted ice thickness under the rime condition would increase linearly as a function of the ice accretion time, evident non-linear features were observed in the ice growth curves derived under the glaze condition.

The measurement results of the aerodynamic drag forces during the dynamic ice accretion processes reveal that, the aerodynamic drag of the standard plain cable and the cable with helical fillet could actually be reduced due to the dynamic ice accretion (i.e., reduced ~25% after 600 s of the ice accretion experiment). However, the drag force acting on the pattern-indented cable model was found to increase during the dynamic icing processes, i.e., increase ~30% after 600 s of the ice accretion experiment. In addition to the changes of the drag coefficient caused by the ice accretion on the cable surfaces, the aeroelastic properties of the cables are also suggested to be significantly affected due to the elongation of the outer profiles of the ice accreting cable models, which may result in further amplified galloping and potential collapse. The findings derived from this study is of great importance in elucidating the underlying icing physics pertinent to bridge cable icing phenomena in cold climates.

Acknowledgments

The research work is partially supported by Iowa Space Grant Consortium (ISGC) Base Program for Aircraft Icing Studies, National Aeronautics and Space Administration (NASA) with the grant number of NNX16AN21A, and National Science Foundation (NSF) under award numbers of CMMI- 1824840 and OISE-1826978.

Appendix A. Supplementary data

Supplementary data to this article can be found online at https://doi.org/10.1016/j.jweia.2019.05.007.

References

Anderson, D.D., 2001. Acceptable tolerances for matching icing similarity parameters in scaling applications. In: AIAA Paper 2001-0832, Aerospace Sciences Meetings. https://doi.org/10.2514/6.2001-832.

Anon, 2013. FAA Federal Aviation Regulations (FAR-25).

Battisti, L., 2015. Wind turbines in cold climates, wind turbines in cold climates. https://doi.org/10.1007/978-3-319-05191-8.

Bosdogianni, A., Olivari, D., 1996. Wind- and rain-induced oscillations of cables of stayed bridges. J. Wind Eng. Ind. Aerodyn. 64, 171–185. https://doi.org/10.1016/S0167-6105(96)00089-X.

Bragg, M.B., Broeren, A.P., Blumenthal, L.A., 2005. Iced-airfoil aerodynamics. Prog. Aero. Sci. 41, 323–362. https://doi.org/10.1016/j.paerosci.2005.07.001.

Barlow, J.B., Rae, J., Pope, A., 1999. Low Speed Wind Tunnel Testing, third ed. ed. Wiley & Sons.

Cao, S., Jalali, H.H., Dragomirescu, E., 2018. Wind-induced response of inclined and yawed ice-accreted stay cable models. Shock Vib. 2018, 1–12. https://doi.org/10.1155/2018/6853047.

Christiansen, H., Jakobsen, J.B., Macdonald, J.H.G., Larose, G.L., Bosch, H.R., 2018. Aerodynamics of a stay cable with helical fillets - Part I: stability and load characteristics. J. Wind Eng. Ind. Aerodyn. 177, 376–391. https://doi.org/10.1016/J.JWEIA.2018.01.045.

Demartino, C., Koss, H.H., Georgakis, C.T., Ricciardelli, F., 2015. Effects of ice accretion on the aerodynamics of bridge cables. J. Wind Eng. Ind. Aerodyn. 138, 98–119. https://doi.org/10.1016/j.jweia.2014.12.010.

Demartino, C., Ricciardelli, F., 2015. Aerodynamic stability of ice-accreted bridge cables. J. Fluids Struct. 52, 81–100. https://doi.org/10.1016/J.JFLUIDSTRUCTS.2014.10.003.

Dong, W., Zhu, J., Zheng, M., Lei, G.L., Zhou, Z.X., 2015. Experimental study on icing and anti-icing characteristics of engine inlet guide vanes. J. Propuls. Power 31, 1330–1337. https://doi.org/10.2514/1.B35679.

Fukusako, S., Horibe, A., Tago, M., 1989. Ice accretion characteristics along a circular cylinder immersed in a cold air stream with seawater spray. Exp. Therm. Fluid Sci. 2, 81–90. https://doi.org/10.1016/0894-1777(89)90052-6.

Gao, L., Liu, Y., Zhou, W., Hu, H., 2019. An experimental study on the aerodynamic performance degradation of a wind turbine blade model induced by ice accretion process. Renew. Energy 133, 663–675. https://doi.org/10.1016/J.RENENE.2018.10.032.

Gent, R.W., Dart, N.P., Cansdale, J.T., 2000. Aircraft icing. Philos. Trans. R. Soc. London. Ser. A Math. Phys. Eng. Sci. 358, 2873–2911.

Gjelstrup, H., Georgakis, C.T., Larsen, A., 2012. An evaluation of iced bridge hanger vibrations through wind tunnel testing and quasi-steady theory. Wind Struct. An Int. J. 15, 385–407. https://doi.org/10.12989/was.2012.15.5.385.

Gu, M., Du, X., 2005. Experimental investigation of rain–wind-induced vibration of cables in cable-stayed bridges and its mitigation. J. Wind Eng. Ind. Aerodyn. 93, 79–95. https://doi.org/10.1016/J.JWEIA.2004.09.003.

Han, Y., Palacios, J., Schmitz, S., 2012. Scaled ice accretion experiments on a rotating wind turbine blade. J. Wind Eng. Ind. Aerodyn. 109, 55–67. https://doi.org/10.1016/j.jweia.2012.06.001.

Hansman, R.J., Kirby, M.S., 1987. Comparison of wet and dry growth in artificial and flight icing conditions. J. Thermophys. Heat Transf. 1, 215–221.

Hansman, R.J., Turnock, S.S.R., 1989. Investigation of surface water behavior during glaze ice accretion. J. Aircr. 26, 140–147.

Hansman, R.J., Yamaguchi, K., Berkowitz, B., Potapczuk, M., 1991. Modeling of surface roughness effects on glaze ice accretion. J. Thermophys. Heat Transf. 5, 54–60.

Hikami, Y., Shiraishi, N., 1988. Rain-wind induced vibrations of cables stayed bridges. J. Wind Eng. Ind. Aerodyn. 29, 409–418. https://doi.org/10.1016/0167-6105(88)90179-1.

Ishihara, T., Oka, S., 2018. A numerical study of the aerodynamic characteristics of ice-accreted transmission lines. J. Wind Eng. Ind. Aerodyn. 177, 60–68. https://doi.org/10.1016/J.JWEIA.2018.04.008.

Kleissl, K., Georgakis, C.T., 2012. Comparison of the aerodynamics of bridge cables with helical fillets and a pattern-indented surface. J. Wind Eng. Ind. Aerodyn. 104–106, 166–175. https://doi.org/10.1016/J.JWEIA.2012.02.031.

Koss, H., Lund, M.S.M., 2013. Experimental investigation of aerodynamic instability of iced bridge cable sections. In: Proceedings of the 6th European and African Wind Engineering Conference. Cambridge, p. 8.

Koss, H.H., Gjelstrup, H., Georgakis, C.T., 2012. Experimental study of ice accretion on circular cylinders at moderate low temperatures. J. Wind Eng. Ind. Aerodyn. 104–106, 540–546. https://doi.org/10.1016/j.jweia.2012.03.024.

Koss, H.H., Henningsen, J.F., Olsen, I., 2013. Influence of Icing on Bridge Cable Aerodynamics. St. John's, Newfoundland and Labrador, Canada.

Li, F.-C., Chen, W.-L., Li, H., Zhang, R., 2010. An ultrasonic transmission thickness measurement system for study of water rivulets characteristics of stay cables suffering from wind–rain-induced vibration. Sensors Actuators A Phys 159, 12–23.

Li, L., Liu, Y., Zhang, Z., Hu, H., 2019. Effects of thermal conductivity of airframe substrate on the dynamic ice accretion process pertinent to UAS inflight icing phenomena. Int. J. Heat Mass Transf. 131, 1184–1195. https://doi.org/10.1016/J.IJHEATMASSTRANSFER.2018.11.132.

Li, Li, Hu, H., 2017. An experimental study of dynamic ice accretion process on aero-engine spinners. In: 55th AIAA Aerospace Sciences Meeting, AIAA SciTech Forum. American Institute of Aeronautics and Astronautics. https://doi.org/10.2514/6.2017-0551.

Liu, B., Ji, K., Zhan, X., Fei, X., Li, P., Zhao, B., Dong, Y., Deng, C., Liu, L., Wang, Z., Luo, Y., Bai, Y., 2017. Experimental and numerical analysis of overhead transmission lines vibration due to atmospheric icing. In: 2017 Prognostics and System Health Management Conference (PHM-Harbin). IEEE, pp. 1–4. https://doi.org/10.1109/PHM.2017.8079288.

Liu, Y., Hu, H., 2018. An experimental investigation on the unsteady heat transfer process over an ice accreting airfoil surface. Int. J. Heat Mass Transf. 122, 707–718. https://doi.org/10.1016/j.ijheatmasstransfer.2018.02.023.

Liu, Y., Li, L., Chen, W., Tian, W., Hu, H., 2019. An experimental study on the aerodynamic performance degradation of a UAS propeller model induced by ice accretion process. Exp. Therm. Fluid Sci. 102, 101–112. https://doi.org/10.1016/J.EXPTHERMFLUSCI.2018.11.008.

Liu, Y., Li, L., Li, H., Hu, H., 2018a. An experimental study of surface wettability effects on dynamic ice accretion process over an UAS propeller model. Aero. Sci. Technol. 73, 164–172. https://doi.org/https://doi.org/10.1016/j.ast.2017.12.003.

Liu, Y., Li, L., Ning, Z., Tian, W., Hu, H., 2018b. Experimental investigation on the dynamic icing process over a rotating propeller model. J. Propuls. Power 0, 1–15. https://doi.org/10.2514/1.B36748.

Liu, Y., Li, L., Ning, Z., Tian, W., Hu, H., 2018c. Experimental investigation on the dynamic icing process over a rotating propeller model. J. Propuls. Power 1–14. https://doi.org/10.2514/1.B36748.

Matsumoto, M., Daito, Y., Kanamura, T., Shigemura, Y., Sakuma, S., Ishizaki, H., 1998. Wind-induced vibration of cables of cable-stayed bridges. J. Wind Eng. Ind. Aerodyn. 74–76, 1015–1027. https://doi.org/10.1016/S0167-6105(98)00093-2.

Matsumoto, M., Saitoh, T., Kitazawa, M., Shirato, H., Nishizaki, T., 1995. Response characteristics of rain-wind induced vibration of stay-cables of cable-stayed bridges. J. Wind Eng. Ind. Aerodyn. 57, 323–333. https://doi.org/10.1016/0167-6105(95)00010-O.

Matsumoto, M., Shiraishi, N., Shirato, H., 1992. Rain-wind induced vibration of cables of cable-stayed bridges. J. Wind Eng. Ind. Aerodyn. 43, 2011–2022. https://doi.org/10.1016/0167-6105(92)90628-N.

Nilanjan, S., 1999. Gap Size Effect on Low Reynolds Number wind Tunnel Experiments. Virginia Tech. Master Thesis.

Papadakis, M., Zumwalt, G.W., Elangonan, R., Freund, G.A.J., Breer, M., Whitmer, L., 1989. An Experimental Method for Measuring Water Droplet Impingement Efficiency on Two- and Three-Dimensional Bodies.

Parent, O., Ilinca, A., 2011. Anti-icing and de-icing techniques for wind turbines: critical review. Cold Reg. Sci. Technol. 65, 88–96. https://doi.org/10.1016/j.coldregions.2010.01.005.

Shin, J., 1996. Characteristics of surface roughness associated with leading-edge ice accretion. J. Aircr. 33, 316–321. https://doi.org/10.2514/3.46940.

Tan, D.-M., Wang, K.-L., Qu, W.-L., Han, L., Gao, Y.-Z., 2016. Galloping analysis of wind-induced vibration for 3D stay cables with iced accretion. Zhendong yu Chongji/Journal Vib. Shock 35. https://doi.org/10.13465/j.cnki.jvs.2016.07.024.

Waldman, R.M., Hu, H., 2015. High-speed imaging to quantify transient ice accretion process over an airfoil. J. Aircr. 53, 369–377. https://doi.org/10.2514/1.C033367.